Available online at www.sciencedirect.com
ScienceDirect
Trans. Nonferrous Met. Soc. China 34(2024) 2772−2786
Transactions of Nonferrous Metals Society of China
www.tnmsc.cn

Corrosion behavior of 2A97 Al−Cu−Li alloys in different thermomechanical conditions by quasi-in-situ analysis

You LÜ, Xiang-zhe MENG, Yan-yan LI, Ze-hua DONG, Xin-xin ZHANG

Hubei Key Laboratory of Material Chemistry and Service Failure, School of Chemistry and Chemical Engineering, Huazhong University of Science and Technology, Wuhan 430074, China

Received 22 March 2023; accepted 24 October 2023

Abstract: As a promising material in the aircraft industry, 2A97 Al−Cu−Li alloy exhibits high corrosion susceptibility that may limit its application. In the present work, to illustrate the influences of precipitate and grain-stored energy on localized corrosion evolution in 2A97 Al−Cu−Li alloy, cold working and artificial aging were carried out to produce 2A97 Al−Cu−Li alloys under different thermomechanical conditions. Quasi-in-situ analysis, traditional immersion test and electrochemical measurement were then conducted to examine the corrosion behavior of 2A97 alloys. It is revealed that precipitate significantly affects Cu enrichment at corrosion fronts, which determines corrosion susceptibility of alloys, whereas grain-stored energy distribution is closely associated with localized corrosion propagation. It is also indicated that quasi-in-situ analysis exhibits a consistent corrosion evolution with traditional immersion tests, which is regarded as a proper method to explore localized corrosion mechanisms by providing local microstructural information with enhanced time and spatial resolutions.

Key words: Al−Cu−Li alloy; corrosion behavior; quasi-in situ analysis; grain-stored energy; thermomechanical treatment

1 Introduction

Lithium (Li) is considered as a promising alloying element in aluminium (Al) to meet the demanding requirements in the aircraft industry [1]. The incorporation of Li into Al could bring the alloy several improvements, including a reduction in density, an increase in the elastic modulus and an enhancement in fatigue crack growth resistance [1−5]. The above-mentioned advantages encourage the development of Al−Cu−Li alloys, which have been widely used as structural components like fuselage wing stringers and floor beams in modern commercial aircraft [6−8].

However, the addition of Li dramatically reduces the corrosion resistance of Al alloys, which can lead to their premature failure and thus compromise the safe operation of Al−Cu−Li-based components in aircraft [9]. Since Li possesses an electrode potential of about −3.04 V (vs SHE), those Li-containing phases generally display higher electrochemical activities relative to Al, which thus promotes the galvanic interaction with the surrounding Al matrix and finally results in localized corrosion development in Al−Cu−Li alloy. Particularly, T_1(Al_2CuLi) phase, as one of the main strengthening precipitates in the new generation Al−Cu−Li alloy, exerts a crucial impact on its corrosion behavior [10−13]. Initially, due to its high Li content, T_1 phase displays a more anodic nature relative to Al matrix. Subsequently, selective

Corresponding author: Xin-xin ZHANG, Tel: +86-27-87541114, E-mail: xinxinzhang@hust.edu.cn
DOI: 10.1016/S1003-6326(24)66575-1
1003-6326/© 2024 The Nonferrous Metals Society of China. Published by Elsevier Ltd & Science Press
This is an open access article under the CC BY-NC-ND license (http://creativecommons.org/licenses/by-nc-nd/4.0/)

dissolution of Li and possibly Al from T_1 phase results in the formation of a Cu-rich remnant and simultaneously leads to the local alkalization, which may promote trenching in its periphery by de-stabilizing the passive film. Afterwards, the Cu-rich remnant could act as an effective cathode to promote the anodic dissolution of the peripheral matrix [14−16]. Hence, the correlation between T_1 phase and corrosion morphology is expected, especially in an artificially-aged Al−Cu−Li alloy with a high volume fraction of T_1 phase [17].

Previous work [18] on a naturally-aged Al−Cu−Li alloy revealed that intergranular corrosion (IGC) tends to occur at grain boundaries free of precipitates with the peripheral boundaries decorated by T_1 phase precipitates remaining intact. This indicates that, in addition to chemical factors, structural factors (like grain boundary misorientation and grain-stored energy) may also influence IGC development in Al−Cu−Li alloys.

Based on grain boundary misorientation, grain boundaries could be divided into two distinctive types, including high-angle grain boundaries (HAGBs, with misorientation higher than 15°) and low-angle grain boundaries (LAGBs, with misorientation higher than 1.5° but lower than 15°), which are believed to affect IGC development in several aluminum alloys [11,19−23]. Generally, due to the high interfacial energy of HAGBs, precipitation preferentially occurs [24], accounting for their higher IGC susceptibility relative to LAGBs [22,25,26], However, in Al−Cu−Li alloys, a different scenario has been reported previously. The work of LIU et al [21] reveals that the precipitation of S' (Al_2CuMg) phase tends to occur at LAGBs whereas T_1 phase is mainly present at HAGBs, thus resulting in their different IGC susceptibility. Similarly, in our previous work, it was noticed that precipitates at LAGBs were finer and more closely packed compared to those at HAGBs, which may lead to the higher IGC susceptibility of LAGBs than HAGBs [24].

In addition to grain boundary misorientation, previous work on 2A97-T3 alloy indicated that attacked grain boundaries (AGBs) tend to locate surrounding grains of higher stored energies and vice versa, indicating the crucial role of stored energy during localized corrosion evolution in Al−Cu−Li alloys [19]. The influence of stored energy on localized corrosion development has been repeatedly reported in Al−Cu−Li and other aluminium alloys, which could be correlated with both intergranular and intragranular corrosion [18,24,27,28]. This suggests that grain structure, especially grain stored energy, exerts a profound influence on the corrosion behavior of Al−Cu−Li alloys.

Since most Al−Cu−Li alloys are supplied in T8 conditions involving both cold working and artificial aging, their corrosion behaviors are influenced by both structural factors and chemical conditions [24,29,30]. However, their individual role during the localized corrosion development remains indecisive. Herein, both cold working and artificial aging were carried out to a representative 3rd generation 2A97 Al−Cu−Li alloy to produce the alloys in T3 (cold-worked), T4 (solution heat treated), T6 (artificially-aged) and T8 (cold-worked and artificially-aged) conditions. By comparing their electrochemical responses and corrosion evolutions via quasi-in-situ examination, the effects of local plastic deformation characterized by grain-stored energy and local precipitation on localized corrosion were discussed to advance the understanding of the localized corrosion mechanism of Al−Cu−Li alloys.

2 Experimental

For producing alloys under different thermo-mechanical conditions, 2A97 Al−Cu−Li alloy (3.48% Cu, 1.35% Li, 0.02% Si, 0.29% Mg, 0.28% Mn, 0.18% Fe and balance Al, in mass fraction) in form of plates with the thickness of ~3 mm was initially subjected to solution heat treatment (SHT) at 540 °C for 5 h. To achieve T3 condition, the cold working (~3%) and the subsequent natural aging process were applied. T4 condition was achieved with the application of the natural aging process directly after SHT. By contrast, the alloy in T6 condition went through artificial aging at 185 °C for 5 h followed by SHT and that in T8 condition required extra cold working (~3%) before artificial aging after SHT.

Specimens obtained from those plates were firstly subjected to mechanical polishing to 1 μm diamond paste, which were then rinsed by ethanol and deionized water, respectively. For micro-structural characterization, electropolishing in the mixture of 30 vol.% perchloric acid and 70 vol.%

ethanol at the temperature of ~10 °C was carried out on mechanically polished alloy surfaces for the subsequent scanning electron microscopy (SEM) examination. To assess their mechanical performances, a microhardness tester with a load of 500 g was employed to measure the microhardness.

For the corrosion behavior, electrochemical measurement, immersion test and quasi-in-situ analysis were all carried out on 2A97 alloys of different thermomechanical treatments. For electrochemical measurements, a de-aerated 3.5 wt.% NaCl solution was used as the testing solution, which was achieved by inputting high-purity nitrogen at the ambient temperature. Open circuit potential (OCP) was recorded during the immersion by a traditional three-electrode configuration [31]. Anodic polarization was then conducted at a scanning speed of 0.5 mV/s after 30 min immersion to achieve a stable OCP. In addition to traditional electrochemical measurements, scanning Kelvin probe force microscopy (SKPFM) was also utilized to measure Volta potentials of those alloys in different thermomechanical conditions. Each experiment was repeated at least three times to ensure the accuracy.

The immersion test was conducted in a 3.5 wt.% NaCl solution for 5 h. Afterwards, the specimens were immediately removed from the solution, rinsed by deionized water and finally dried in a cool air stream. Gentle polishing with 1 μm diamond paste was applied to remove the corrosion product on the alloy surface, which was then cleaned by a glow discharge optical emission spectrometry (GDOS) to prepare a proper surface condition for the measurements using SEM and electron backscatter diffraction (EBSD).

For quasi-in-situ analysis, electron-transparent foils of 2A97 alloys were employed, which were prepared by twin-jet electropolishing using a mixture of 700 mL methanol and 300 mL nitric acid at the temperature of about −30 °C. To avoid potential contaminations like Cu deposition, the solution was refreshed after the electropolishing to ensure its low concentration of Cu ions. SEM observation was conducted before and after immersing the foils in a dilute NaCl solution (0.01 mol/L) for certain periods to determine the corrosion morphological evolution. Afterwards, microstructural features of representative localized corrosion fronts were examined by transmission electron microscopy (TEM) and transmission Kikuchi diffraction (TKD) analysis.

3 Results

3.1 Microstructure

Figure 1 exhibits representative SEM microstructures of electropolished specimens. The distribution of precipitates in alloys in different thermomechanical conditions can be clearly illustrated. A typical area on the surface of 2A97-T3 alloy is shown in Fig. 1(a), which displays several submicron-sized bright features, namely precipitates, at the grain boundary rather than within the grain interior [19], indicating that precipitation in T3 alloy tends to occur at grain boundary rather than within the matrix. Similarly, in T4 alloy (Fig. 1(b)), precipitates are almost absent within the grain interior with only a few fine precipitates detected at the grain boundary [18].

In contrast to T3 and T4 alloys, T6 and T8 alloys exhibit much higher population densities of precipitates due to the application of artificial aging. Figure 1(c) exhibits a typical grain boundary on the surface of T6 alloy with a magnified view inset, which reveals the presence of needle-shaped precipitates within the grain interior and along the grain boundary network. These needle-shaped precipitates are T_1 phase and θ' phase (Al_2Cu) on habit planes of $\{111\}_{Al}$ and $\{001\}_{Al}$ as documented previously [24,32]. The distribution of precipitates in T8 alloy (Fig. 1(d)) remains similar to that of T6 alloy, which exhibits a high population density of needle-shaped precipitates within grain interior (inset in Fig. 1(d)) as well as at grain boundaries [24]. TEM characterization of 2A97 alloys in different thermomechanical conditions has been systematically carried out with representative results reported previously [16,19,24,28,32], thus providing more detailed microstructural information on these alloys.

Following the microstructural characterization, microhardness measurements were carried out on 2A97 alloys at different annealing temperatures to compare their mechanical strength (Fig. 2). The T4 alloy has the lowest microhardness of ~HV 112. The additional cold working before natural aging dramatically increases the microhardness of T3 alloy to ~HV 140. Artificial aging results in a

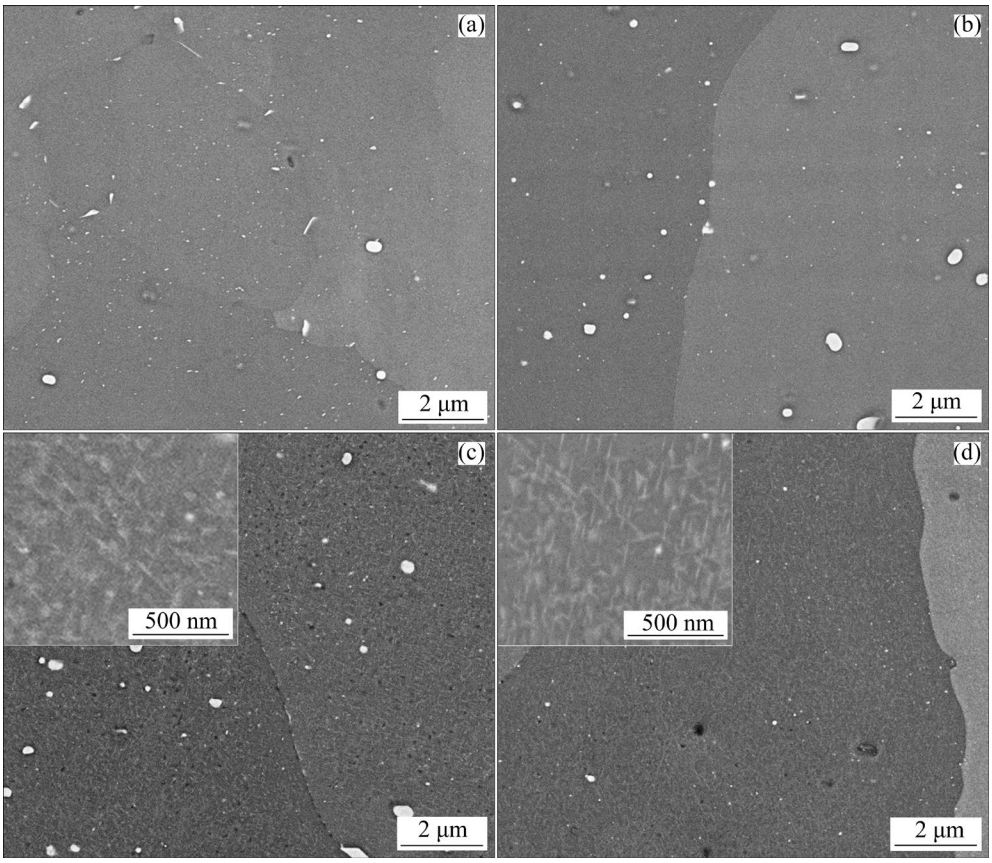

Fig. 1 SEM images of 2A97 alloys in different thermomechanical conditions, revealing distribution of precipitates: (a) T3 alloy; (b) T4 alloy; (c) T6 alloy; (d) T8 alloy

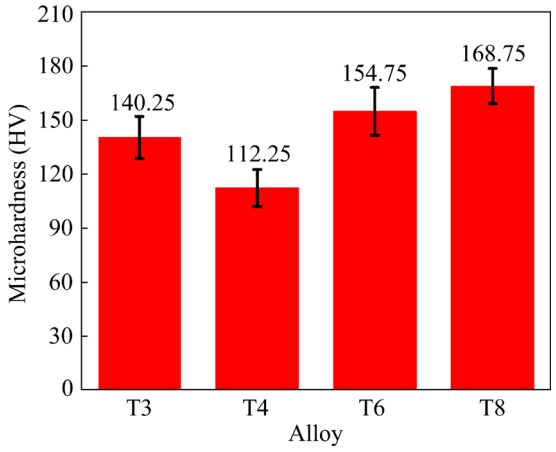

Fig. 2 Microhardness of 2A97 alloys in different thermo-mechanical conditions

higher microhardness value of HV ~155 for T6 alloy. The extra cold working before artificial aging further promotes the increase in microhardness to HV ~169 for T8 alloy. Hence, the microhardness follows a decreasing sequence: T8>T6>T3>T4. Interestingly, the difference in microhardness between T6 and T8 alloys is less significant than that between T4 and T3 alloys, indicating that cold working and artificial aging unequally affect the mechanical performances of Al−Cu−Li alloys.

3.2 Electrochemical properties

Electrochemical measurements were carried out on 2A97 Al−Cu−Li alloys in various thermo-mechanical conditions (Figs. 3 and 4). Figure 3 shows the variations of the Volta potentials across the alloys. The T8 alloy shows the highest Volta potential of ~143 mV and the T4 alloy shows the lowest value of ~80 mV, while those for the T3 (~97 mV) and T6 (~112 mV) alloys are in-between. As the variation of the Volta potential reflects the micro-galvanic coupling across the alloy, it could be considered as an indicator of its corrosion susceptibility, suggesting that the corrosion susceptibility follows the decreasing sequence: T8>T6>T3>T4.

Figure 4(a) shows the evolution of the open circuit potentials (OCPs) over the immersion periods for all examined alloys. The potential−time curves follow a similar tendency, which initially moves towards a negative position, then gradually

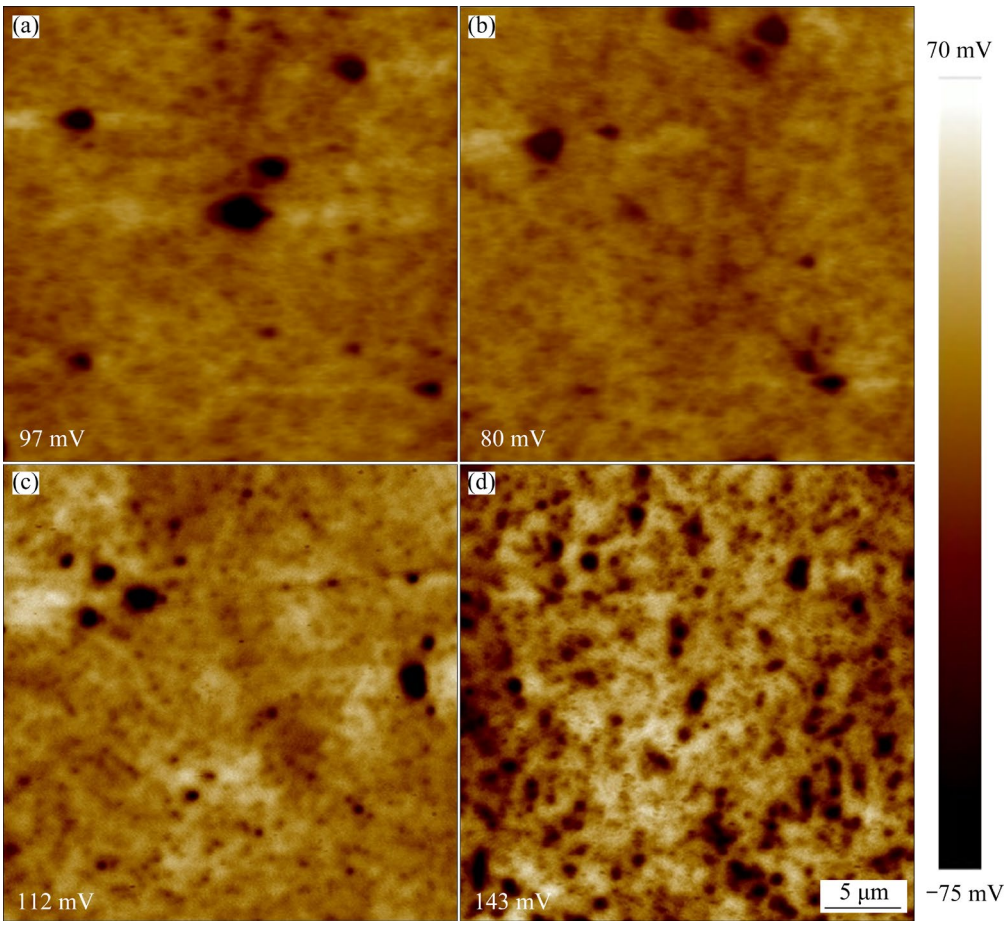

Fig. 3 SKPFM analysis results of alloys in different thermomechanical conditions: (a) T3 alloy; (b) T4 alloy; (c) T6 alloy; (d) T8 alloy (The values inset indicate the variations of Volta potentials, namely the differences between the maximum values and the minimum values of the examined areas)

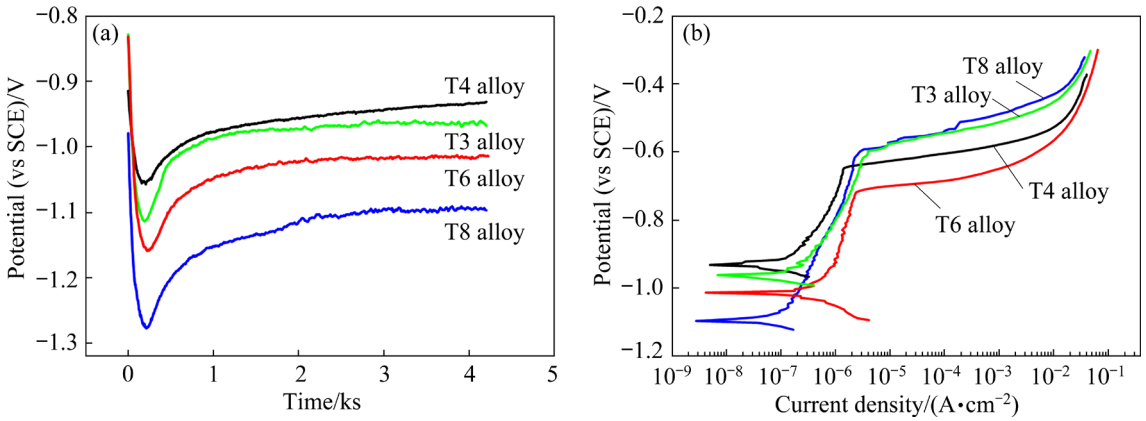

Fig. 4 Electrochemical measurement results of 2A97 alloys in different thermomechanical conditions: (a) Open circuit potential; (b) Potentiodynamic polarization curves

increases, and finally reaches a stable value. Considering the similar distribution and chemical compositions of intermetallic particles in 2A97 alloys of all thermomechanical treatments, the OCP is regarded as an indicator of the corrosion susceptibility of the examined alloy [22]. The OCP value is obtained by averaging all the data collected during the last 10 min, which follows a decreasing sequence: T4>T3>T6>T8 (listed in Table 1), thus indicating a reversed sequence of corrosion

Table 1 Open circuit potentials of 2A97 alloys

Sample	T3	T4	T6	T8
OCP (vs SCE)/V	−0.96±0.02	−0.93±0.01	−1.01±0.01	−1.10±0.01

susceptibility: T8>T6>T3>T4.

Potentiodynamic polarization curves of 2A97 alloys are shown in Fig. 4(b), again displaying similar shapes. After an almost linear increase in current density, a relatively stable current density corresponding to the passive stage is observed. When the external voltage increases to the pitting potential, a sudden increase in current density occurs, corresponding to the de-passivation. The alloy is then subjected to extensive anodic dissolution promoted by the external voltage. The current densities of alloys are comparable at the same over-potentials whereas the corrosion potentials of alloys are dramatically different, which thus indicates a decreasing sequence of corrosion susceptibility based on corrosion potentials: T8>T6>T3>T4. Therefore, both OCP and PDP results (Fig. 4) indicate that the corrosion susceptibility of 2A97 alloys follows the sequence: T8>T6>T3>T4, which is consistent with that of the Volta potential variation (Fig. 3).

3.3 Traditional immersion test results

Following the electrochemical measurements, the immersion test in a 3.5 wt.% NaCl solution was conducted. Typical localized corrosion sites after 5 h immersion were examined by SEM and EBSD to correlate the grain-stored energy with the corrosion propagation path. A typical localized corrosion site in T3 alloy is shown in Fig. 5(a_1) with the framed area magnified in Fig. 5(a_2). Narrow and dark bands, supposed to be AGBs, are observed, indicating the occurrence of IGC in T3 alloy. Interestingly, the widths of the AGBs are uneven, which indicates that IGC may propagate into the grain interior as reported previously [19,27]. Furthermore, the area of Fig. 5(a_1) is examined by EBSD analysis with the reconstructed maps shown in Figs. 5(a_3) and (a_4). Figure 5(a_3) displays the grain orientation distribution in Euler's color, confirming that the narrow and dark bands are AGBs. The corresponding distribution of grain-stored energy in greyscale is shown in Fig. 5(a_4). By comparing Figs. 5(a_1) and (a_4), it is revealed that localized corrosion tends to occur in the non-recrystallized region of high stored energy and vice versa, successfully correlating IGC susceptibility with stored energy distribution.

Similarly, in T4 alloy, the SEM micrograph of a typical localized corrosion site is shown in Fig. 5(b_1) with the framed area magnified in Fig. 5(b_2). Similar to T3 alloy, narrow and dark bands are present in T4 alloy (Fig. 5(b_2)), which are confirmed to be AGBs by comparing with the orientation distribution map in Euler's color (Fig. 5(b_3)). The distribution of the stored energy in greyscale is shown in Fig. 5(b_4). To correlate the stored energy distribution with the IGC propagation path, Figs. 5(b_1) and (b_4) are compared, indicating the preferential dissolution of grain boundaries surrounding grain with higher stored energy relative to those around grain with lower stored energy. In other words, when a grain exhibits a higher stored energy, the grain boundary in its periphery possesses a higher IGC susceptibility and vice versa, correlating IGC susceptibility with stored energy distribution.

A typical localized corrosion site in T6 alloy is marked by a white arrow in Fig. 5(c_1) with its detailed corrosion morphology shown in Fig. 5(c_2), which clearly shows corroded bands at the site [28,32]. Figure 5(c_3) displays the grain orientation distribution of the region in Euler's color with the frame corresponding to Fig. 5(c_1), indicating that the localized corrosion of T6 alloy (marked by a white arrow in Fig. 5(c_3)) is confined to grain interior. The corresponding stored energy map is then determined and displayed as a greyscale map in Fig. 5(c_4) with the localized corrosion site marked by a white arrow. By comparing Figs. 5(c_1) and (c_4), localized corrosion tends to dissolve the interior of the grain with a higher level of stored energy, leaving that of a lower level of stored energy unattached. Therefore, in the T6 alloy, selective dissolution of grain interior preferentially occurs in grains with higher stored energy, correlating stored energy distribution with the corrosion susceptibility of individual grains in T6 alloy.

A representative localized corrosion site in T8

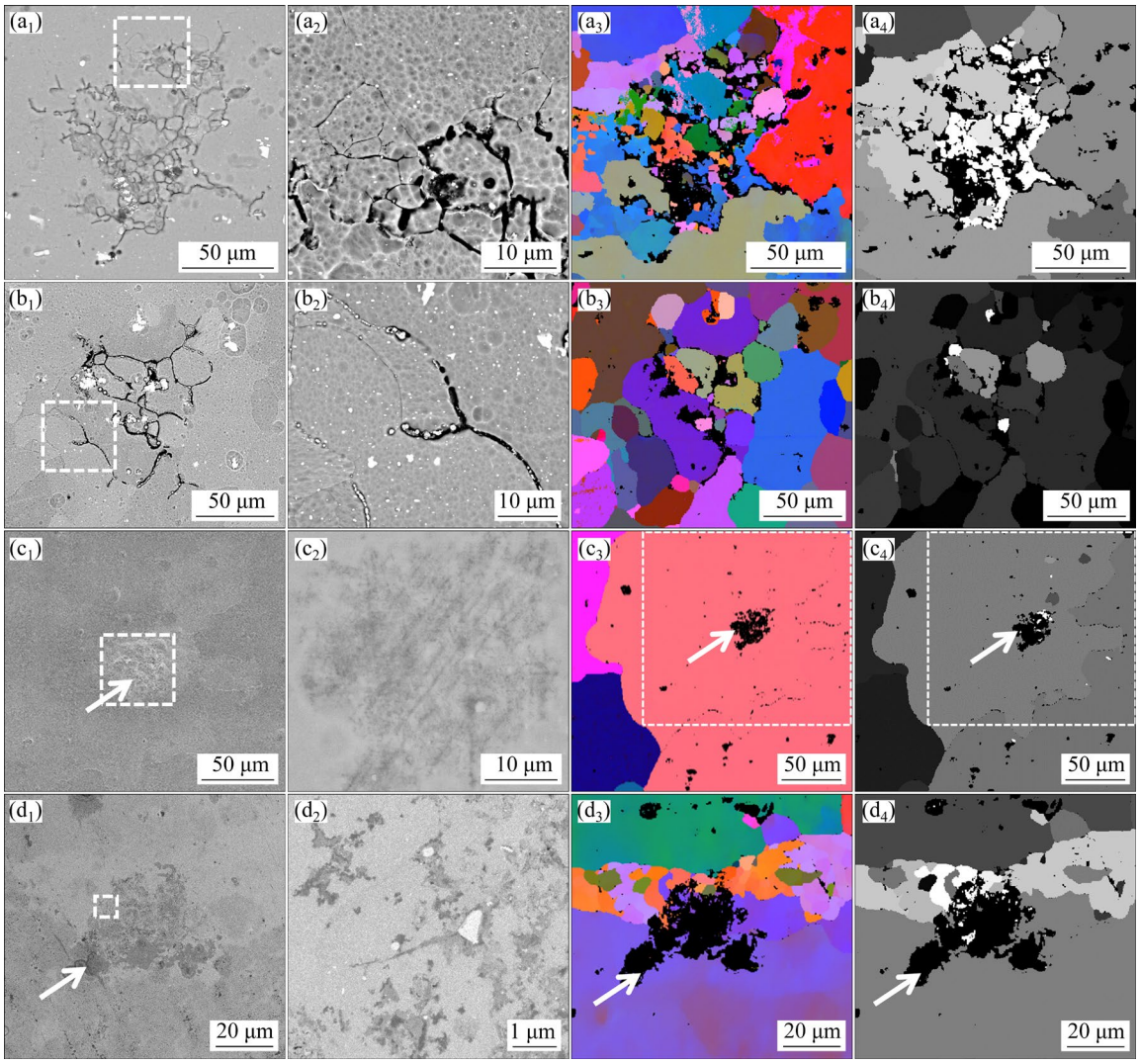

Fig. 5 EBSD analysis results of localized corrosion to correlate corrosion morphology with grain-stored energy: (a_1−a_4) T3 alloy; (b_1−b_4) T4 alloy; (c_1−c_4) T6 alloy; (d_1−d_4) T8 alloy; (a_1−d_1) Typical localized corrosion site; (a_2−d_2) Magnified images of framed areas in (a_1−d_1), respectively; (a_3−d_3) Grain orientation distribution in Euler's color; (a_4−d_4) Grain-stored energy distribution in greyscale

alloy is shown in Fig. 5(d_1) with a typical corrosion front area shown in Fig. 5(d_2), revealing the selective attack of both grain boundary and grain interior during the immersion test. The corresponding distributions of grain orientation in Euler's color and grain-stored energy in greyscale are shown in Figs. 5(d_3) and (d_4), respectively. Comparing Fig. 5(d_1) with Figs. 5(d_3) and (d_4), it is revealed that localized corrosion tends to develop across individual grains in non-recrystallized regions with higher stored energies rather than recrystallized regions of relatively low stored energies. Hence, for T8 alloy, localized corrosion tends to occur in the area of relatively high stored energy.

3.4 Quasi-in-situ analysis results

Unlike the traditional immersion test using bulk specimens and a standard 3.5 wt.% NaCl solution, electron-transparent foils prepared by twin-jet electropolishing were applied during the quasi-in-situ analysis. Considering the low thickness of the electron transparent foil, a diluted NaCl solution (0.01 mol/L) was used as the testing solution [24]. Before the immersion, the morphology of the as-received foil was recorded by SEM and after the immersion, and the same location was re-examined by SEM. Afterwards, the localized corrosion sites were then subjected to TEM and TKD analysis if necessary (Figs. 6−9).

Figures 6(a_1−a_3) exhibit the general view of a

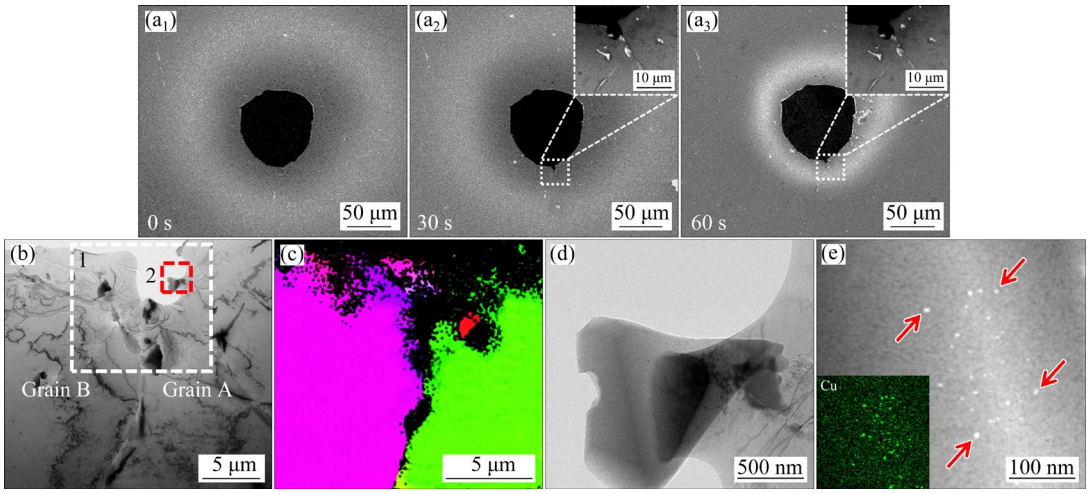

Fig. 6 Quasi-in-situ analysis results of T3 alloy: (a_1−a_3) SEM images of foil before and after immersion in 0.01 mol/L NaCl solution for 30 and 60 s with insects of magnified framed area inset; (b) TEM image of typical localized corrosion after 60 s immersion; (c) TKD image of framed Area 1 in (b); (d) TEM image of framed Area 2 in (b); (e) HAADF image of (d) along with Cu EDX map inset

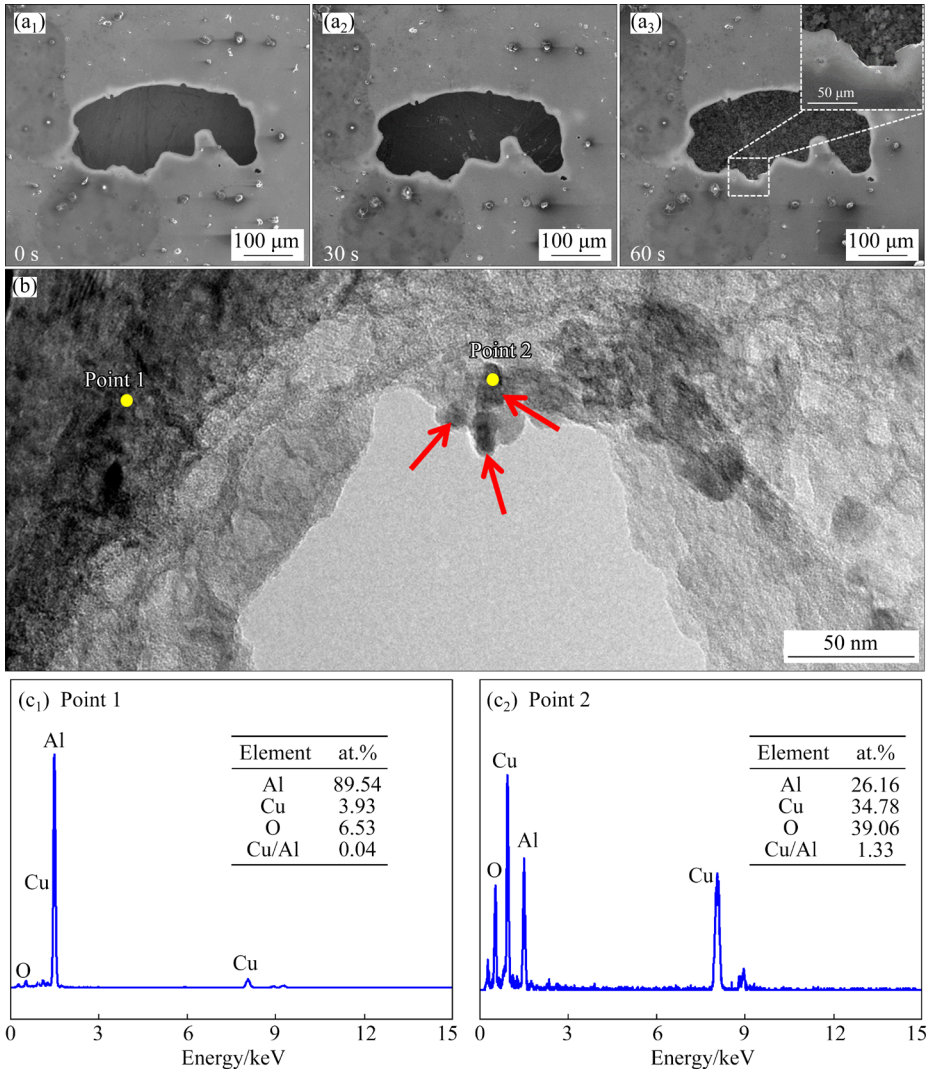

Fig. 7 Quasi-in-situ analysis results of T4 alloy: (a_1−a_3) SEM images of foil before and after immersion in 0.01 mol/L NaCl solution for 30 and 60 s with magnified framed area insets; (b) TEM image of typical localized corrosion area; (c_1, c_2) Typical EDX spectra from Points 1 and 2 in (b) with insets of quantified elemental results, respectively

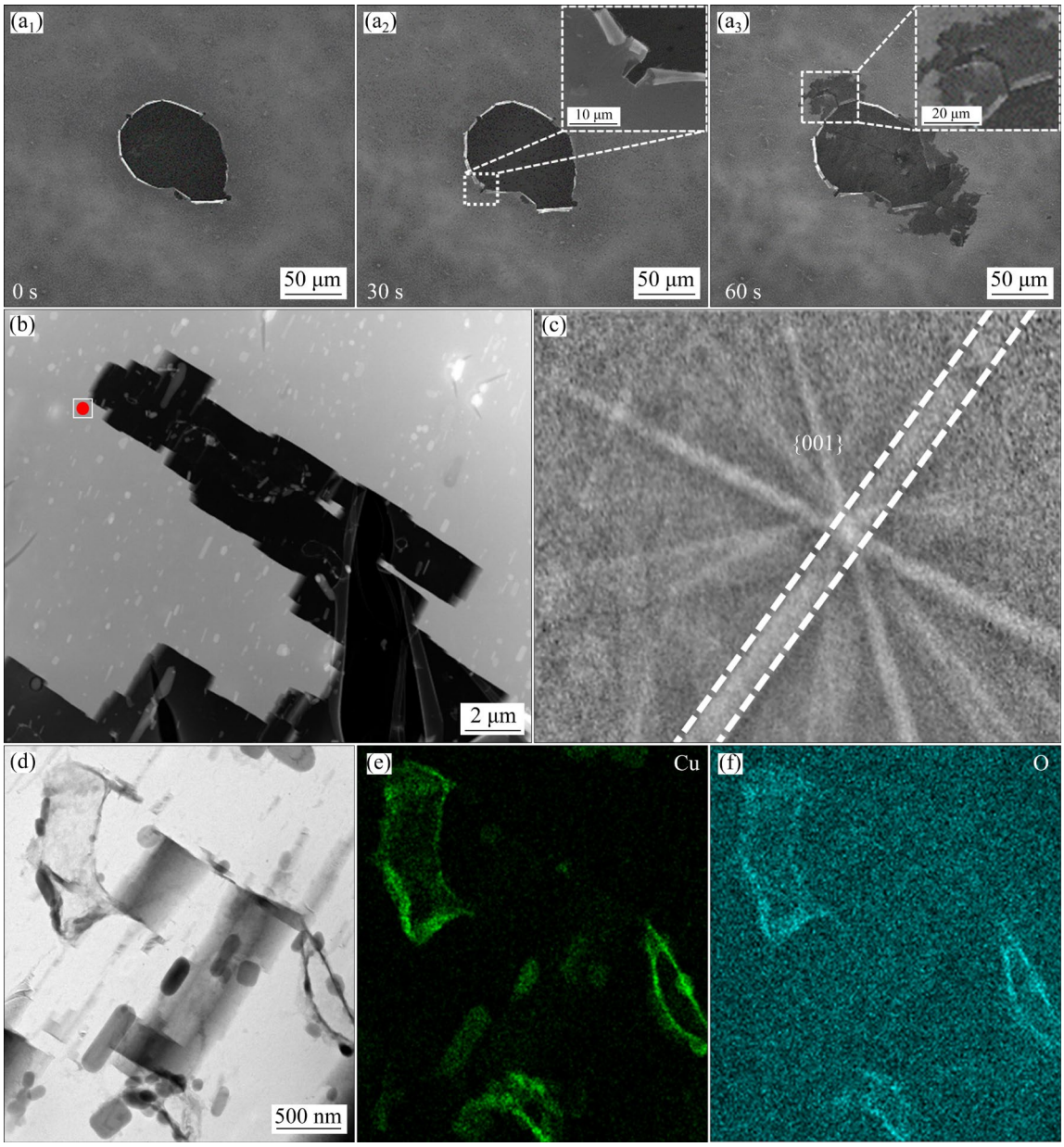

Fig. 8 Quasi-in-situ analysis results of T6 alloy: (a_1−a_3) SEM images of foil before and after immersion in 0.01 mol/L NaCl solution for 30 and 60 s with insets of magnified framed areas; (b) SEM image of typical localized corrosion site after 60 s immersion; (c) Corresponding Kikuchi pattern from marked point in (b); (d) Bright field TEM image of typical localized corrosion site; (e) Cu and O EDX maps of (d)

T3 alloy foil before and after immersion in a diluted NaCl solution for 30 and 60 s. The framed areas in Figs. 6(a_2) and (a_3) are magnified, which displays the formation of a dark band during the quasi-in-situ analysis. The dark band is then examined by TEM (Fig. 6(b)) with framed Area 1 subjected to TKD analysis (Fig. 6(c)). In contrast to the relatively low spatial resolution of EBSD (Fig. 5), TKD analysis confirms that the dark band is an AGB. The non-uniform attack of neighboring grains next to the AGB is also evident with Grain A being preferentially dissolved, which is expected to possess a higher level of stored energy relative to Grain B (Fig. 6(b)). The framed Area 2 of Fig. 6(b) is shown in Fig. 6(d), displaying an attacked particle. A magnified high-angle annular dark field (HAADF) micrograph of the particle is shown in Fig. 6(e), which displays a spongy morphology typical for de-alloying. Furthermore, several nano-sized bright features (marked by red arrows in Fig. 6(e)) could also be detected. EDX mapping analysis is then conducted on the area shown in

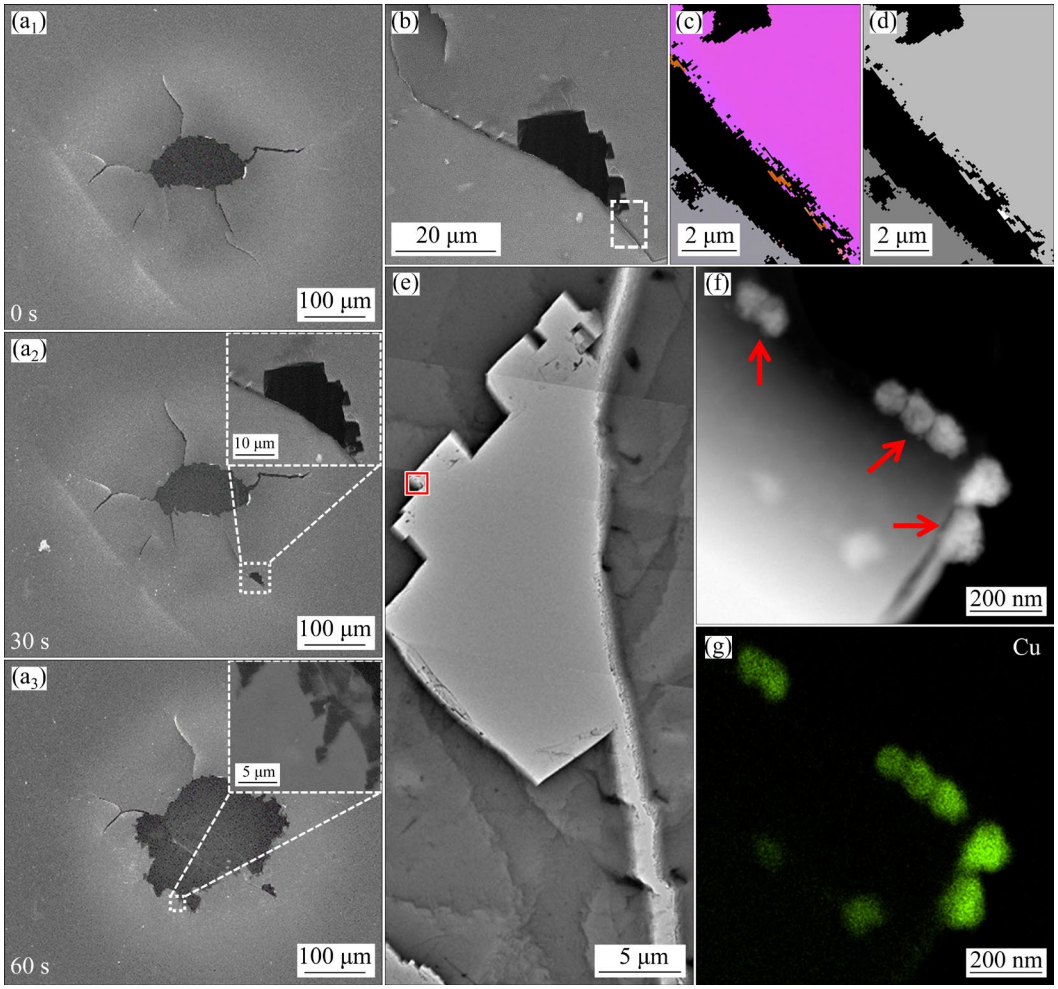

Fig. 9 Quasi-in-situ analysis results of T8 alloy: (a_1−a_3) SEM images of foil before and after immersion in 0.01 mol/L NaCl solution for 30 and 60 s with magnified framed areas inset; (b) High-resolution SEM image of corrosion site after 30 s immersion; (c, d) Grain orientation distribution and grain-stored energy distribution of framed area in (b), respectively; (e) TEM image of marked area in (a_2); (f, g) TEM image of framed area in (e) and its Cu EDX map, respectively

Fig. 6(e) with the EDX map inset of Cu. All nano-sized bright features are rich in Cu, indicating the formation of Cu-rich nano-sized particles, presumably the mixture of metallic Cu and Cu oxides [12,13,33].

Figure 7 exhibits the corrosion morphological evolution of T4 alloy during the quasi-in-situ analysis. Interestingly, after immersion for 30 s, no distinctive corrosion features could be noticed. Only when the immersion period was extended to 60 s, morphological modification induced by corrosion could be noticed (Figs. 7(a_1−a_3)). The attacked area was then subjected to TEM examination (Fig. 7(b)), revealing the presence of several nano-sized particles (marked by red arrows) at the corrosion front. EDX point analysis was then conducted on the nano-sized particles with the surrounding matrix as a comparison. Typical EDX spectra from Points 1 and 2 in Fig. 7(b) are shown in Figs. 7(c_1, c_2) with the quantified results inset. A much higher Cu/Al molar ratio is revealed in these nano-sized particles (Point 2) compared to the alloy matrix (Point 1), indicating their Cu-rich nature. Hence, Cu enrichment is observed at the corrosion front as nano-sized particles in T4 alloy.

The quasi-in-situ analysis was then carried out on T6 alloy (Fig. 8). Figures 8(a_1−a_3) exhibit SEM micrographs of the foil before and after immersion for 30 and 60 s with the magnified framed area inset. Selective dissolution of grain interior tends to occur in the alloy and the attacked area extends with the prolongation of immersion period. Figure 8(b) shows a typical corrosion front in T6 alloy, which exhibits well-defined step-like pit

walls. The Kikuchi pattern is then obtained from the marked location in Fig. 8(b) using TKD (Fig. 8(c)), revealing that the pit wall tends to be on $\{001\}_{Al}$ plane, which thus indicates crystallographic dissolution of the alloy matrix [31]. Figure 8(d) displays a bright field TEM image of a typical localized corrosion site, which is then subjected to EDX mapping analysis. The corresponding EDX maps of O and Cu are shown in Figs. 8(e, f), revealing that Cu enrichment exists accompanied by O-rich corrosion product, which may be ascribed to the embedding of Cu-rich particles within corrosion product [33−35].

Finally, the localized corrosion evolution of T8 alloy was examined by quasi-in-situ analysis (Fig. 9). Comparing SEM images of the foil before and after 30 s immersion (Figs. 9(a_1) and (a_2)), a micro-sized pit is observed next to a dark and narrow band, which is then examined by the combination of high-resolution SEM and TKD (Figs. 9(b, d)). The step-like walls surrounding the pit are clearly revealed (Fig. 9(b)), indicating the occurrence of crystallographic dissolution. The orientation distribution in Euler's color confirms that the dark and narrow band (Fig. 9(b)) is an AGB (Fig. 9(c)). As shown in the stored energy map based on TKD analysis (Fig. 9(d)), it is indicated that selective dissolution of grain interior tends to initiate at AGB and then propagates into grain interior of higher stored energy. It is worth mentioning that the IGC development in the electron transparent foil of T8 alloy seems to be inhibited, which is mainly ascribed to the boundary attack during the twin-jet electropolishing (Fig. 9(a_1)). Hence, a reduced number of grain boundaries are available for the immersion in a dilute NaCl solution, resulting in the preferential dissolution of the grain interior next to the existing AGBs during the quasi-in-situ analysis. Furthermore, the micro-sized pit is examined by TEM, again displaying the step-like crevice walls (Fig. 9(e)) with the framed area magnified in Fig. 9(f). As shown in Fig. 9(f), nano-sized spherical particles, which appears as bright features (marked by red arrows), are present on the crevice walls. EDX mapping is then conducted on the area in Fig. 9(f), which confirms that those nano-sized particles are Cu-enriched (Fig. 9(g)). Afterwards, the foil is further immersed in the diluted NaCl for another 30 s with the general view shown in Fig. 9(a_3). After the immersion for 60 s, localized corrosion extends rapidly in the alloy, thus resulting in extensive dissolution of the foil with obvious crystallographic features.

4 Discussion

4.1 Comparison between traditional immersion test and quasi-in-situ test

Compared with the immersion test results (Fig. 5) [19,24,32,36,37], the quasi-in-situ analysis results generally exhibit comparable corrosion morphological evolution (Figs. 6−9) with only 2A97-T4 alloy showing a slight inconsistency (Fig. 7). For 2A97-T4 alloy, localized corrosion initially develops as IGC and then propagates to the grain interior with higher stored energy during the immersion test [18] even T4 alloy shows mainly general corrosion with only a few localized corrosion sites detected. By contrast, during the quasi-in-situ analysis, only uniform corrosion is observed (Fig. 7). Hence, the difference in corrosion morphological evolution in T4 alloy may be related to the examined volumes.

The specimens of quasi-in-situ analysis could be easily examined by TEM and TKD for a more detailed microstructural characterization (Figs. 6−9) to broaden the understanding of the corrosion process, thus showing obvious advantages over the traditional immersion test (Fig. 5). Considering the comparable corrosion evolution between quasi-in-situ test and traditional immersion test as well as the convenience for detailed microstructural characterization, it is thus indicated that quasi-in-situ analysis could be a powerful tool to study the localized corrosion mechanism in aluminium alloys.

4.2 Influence of precipitates on localized corrosion behavior

The examination of the corrosion fronts produced during the quasi-in-situ test shows that Cu enrichment, mainly in the form of nano-sized particles, is present in all examined corrosion fronts (Figs. 6−9). When exposed to the aggressive external electrolyte, selective dissolution of Li from Li- and Cu-containing precipitates leads to the formation of Cu-rich remnants, which may also promote the formation of nano-sized Cu-rich particles in the periphery via the re-distribution and

re-deposition of Cu species [12,13,33,35]. Generally, the corrosion of aluminium is considered to be catholically limited [15,16,38,39]. Hence, nano-sized Cu-rich particles with a more positive electrode potential and a higher cathodic current density relative to the alloy matrix [10,11,14,40] could act as effective cathodes to promote the anodic dissolution of Al, which dramatically affects the localized corrosion susceptibility. As mentioned above, since the evolution of Cu enrichment is associated with precipitates in the alloy, its corrosion susceptibility is sensitive to the thermo-mechanical treatment that determines the distribution and population density of the precipitates (Fig. 1). As a result, the corrosion sensitivity of Al−Cu−Li alloys in different thermo-mechanical conditions is closely associated with precipitation.

4.3 Influence of stored energy on localized corrosion behavior

For stored energy, it is reported that after different levels of deformation, pure Al exhibits limited changes in electrochemical responses [41] whereas the electrochemical modification related to precipitation and Cu enrichment could be much more significant (ranging from 80 to 400 mV [42]). Moreover, it is also revealed that the influence of plastic deformation on corrosion susceptibility is much more pronounced in precipitation-hardening Al alloy [18,19,23,27] relative to that in pure Al, which is almost negligible [43−45]. It is thus indicated that stored energy may not directly affect the electrochemical response, which fails to affect corrosion sensitivity individually, especially for the alloy with only a low level of plastic deformation. Hence, it is reasonable to deduce that stored energy mainly affects corrosion behavior in precipitation-hardening Al alloy by indirectly affecting precipitation, since a high stored energy reflects a high dislocation density that promotes precipitation and vice versa [24]. Therefore, precipitation may play a more critical role in the corrosion susceptibility of the Al−Cu−Li alloy relative to the stored energy.

Instead, it is believed that grain-stored energy plays a more crucial role during localized corrosion propagation (Fig. 5) [18,19,23]. Obviously, the distribution of precipitates is inconsistent with the corrosion morphology of 2A97 alloys (Figs. 1 and 5−9). For example, even with a high population density of precipitates at grain boundaries in 2A97-T6 alloy (Fig. 1), grain boundaries remain almost intact during both immersion test and quasi-in-situ test with only selective dissolution occurring at grain interiors (Figs. 5 and 8). By contrast, it is clear that localized corrosion tends to occur in the regions with higher levels of stored energies with those of lower stored energies remaining intact [28] (Fig. 5). Unlike corrosion sensitivity, localized corrosion propagation is mainly associated with the local variations of micro-electrochemical properties across the alloy (Fig. 3). As reported previously [24,30,36], grain-stored energy mainly reflects local deformation and also affects the subsequent precipitation. The above-mentioned two factors synergistically determine the micro-electrochemical property, which consequently affects the propagation path of localized corrosion. Hence, grain-stored energy mainly affects the localized corrosion propagation in 2A97 alloys.

5 Conclusions

(1) Precipitates significantly affect the corrosion susceptibility of Al−Cu−Li alloy whereas stored energy mainly affects the propagation of localized corrosion.

(2) Cu enrichment was noticed at corrosion fronts as nano-sized particles, which may act as an effective cathode to stimulate the anodic dissolution of Al. Hence, the correlation between precipitation and corrosion sensitivity of Al−Cu−Li alloy is established since Cu enrichment at the corrosion front is dramatically affected by precipitates.

(3) Localized corrosion tends to occur within the area of higher stored energy, whereas the area of lower stored energy remains intact. As a result, the corrosion propagation path is closely associated with the stored energy distribution.

(4) Generally, quasi-in-situ analysis exhibits a consistent corrosion morphological evolution with traditional immersion test. Moreover, quasi-in-situ analysis could provide local microstructural information at corrosion fronts with both enhanced time and spatial resolutions compared to the traditional immersion test. Hence, it is believed that quasi-in-situ analysis is beneficial to the determination of localized corrosion mechanism.

CRediT authorship contribution statement

You LÜ: Methodology, Formal analysis, Writing − Original draft; **Xiang-zhe MENG:** Formal analysis, Validation; **Yan-yan LI:** Writing − Review & editing; **Ze-hua DONG:** Funding acquisition; **Xin-xin ZHANG:** Conceptualization, Resources, Writing − Review & editing.

Declaration of competing interest

The authors declare that they have no known competing financial interests or personal relationships that could have appeared to influence the work reported in this paper.

Acknowledgments

The authors would like to thank the supports from the National Natural Science Foundation of China (Nos. 52371065, 52001128), and the Hubei Provincial Natural Science Foundation of China (No. 2023AFB637). The authors also would like to thank the technical support from XFNANO Company (Nanjing, China), Shiyanjia Lab, China (www.shiyanjia.com), the Instrumental Analysis & Research Centre of Shanghai Yanku (www.shuyanku.com), the Analytical and Testing Centre in Huazhong University of Science and Technology (HUST), China, the Center of Optoelectronic Micro&Nano Fabrication and Characterizing Facility, Wuhan National Laboratory for Optoelectronics of HUST, China, and the Experiment Centre for Advanced Manufacturing and Technology in School of Mechanical Science and Engineering of HUST, China.

References

[1] MARTIN J W. Aluminum−lithium alloys [J]. Annual Review of Materials Science, 1988, 18: 101−119.

[2] RIOJA R J, LIU J. The evolution of Al−Li base products for aerospace and space applications [J]. Metallurgical and Materials Transactions A, 2012, 43: 3325−3337.

[3] LIN Ben, MA Peng-cheng, LI Hao-ran, DENG San-xi, ZENG Guang-jun, TANG Jian-guo, LI Jin-feng, LI Xi-wu. Anisotropy of Al−Li alloy plate and its heredity effect in mechanical property distribution of spun-dome [J]. Transactions of Nonferrous Metals Society of China, 2023, 33: 1318−1330.

[4] LU Ding-ding, LI Jin-feng, NING Hong, MA Peng-cheng, CHEN Yong-lai, ZHANG Xu-hu, ZHANG Kai, LI Jian-mei, ZHANG Rui-feng. Effects of microstructure on tensile properties of AA2050-T84 Al−Li alloy [J]. Transactions of Nonferrous Metals Society of China, 2021, 31: 1189−1204.

[5] LI Chang, XIONG Han-qing, BHATTA L, WANG Lin, ZHANG Zhao-yang, WANG Hui, KONG C, YU Hai-liang. Microstructure evolution and mechanical properties of Al−3.6Cu−1Li alloy via cryorolling and aging [J]. Transactions of Nonferrous Metals Society of China, 2020, 30: 2904−2914.

[6] ZHAO Xin-yue, LIU Wen-sheng, XIAO Dai-hong, MA Yun-zhu, HUANG Lan-ping, TANG Ya. A critical review: Crystal structure, evolution and interaction mechanism with dislocations of nano precipitates in Al−Li alloys [J]. Materials & Design, 2022, 217: 110629.

[7] DURSUN T, SOUTIS C. Recent developments in advanced aircraft aluminium alloys [J]. Materials & Design, 2014, 56: 862−871.

[8] LIU Dan-yang, MA Yun-long, LI Jin-feng, HUANG Cheng, WANG Yang, WANG Zhi-xiu, ZHANG Rui-feng. The influence of Zn addition on microstructure of an Al−1.7Cu−4.0Li−0.4 Mg alloy [J]. Journal of Materials Research and Technology, 2020, 9: 2423−2439.

[9] CARRICK D M, HOGG S C, WILCOX G D. Influence of Li additions on the microstructure and corrosion response of 2xxx series aluminium alloys [J]. Materials Science Forum, 2014, 794/795/796: 193−198.

[10] ZHU Y K, POPLAWSKY J D, LI S R, UNOCIC R R, BLAND L G, TAYLOR C D, LOCKE J S, MARQUIS E A, FRANKEL G S. Localized corrosion at nm-scale hardening precipitates in Al−Cu−Li alloys [J]. Acta Materialia, 2020, 189: 204−213.

[11] XU X, HAO M, CHEN J, HE W, LI G, LI K, JIAO C, ZHONG X L, MOORE K L, BURNETT T L, ZHOU X. Role of constituent intermetallic phases and precipitates in initiation and propagation of intergranular corrosion of an Al−Li−Cu−Mg alloy [J]. Corrosion Science, 2022, 201: 110294.

[12] ZHANG X X, HASHIMOTO T, LINDSAY J, ZHOU X R. Investigation of the de-alloying behaviour of θ-phase(Al_2Cu) in AA2024-T351 aluminium alloy [J]. Corrosion Science, 2016, 108: 85−93.

[13] HASHIMOTO T, ZHANG X, ZHOU X, SKELDON P, HAIGH S J, THOMPSON G E Investigation of dealloying of *S* phase (Al_2CuMg) in AA 2024-T3 aluminium alloy using high resolution 2D and 3D electron imaging [J]. Corrosion Science, 2016, 103: 157−164.

[14] ZHANG Xin-xin, LV You, TAN Si-han, DONG Ze-hua, ZHOU Xiao-rong. Microstructure and corrosion behaviour of wire arc additive manufactured AA2024 alloy thin wall structure [J]. Corrosion Science, 2021, 186: 109453.

[15] ZHOU X R, LUO C, HASHIMOTO T, HUGHES A E, THOMPSON G E. Study of localized corrosion in AA2024 aluminium alloy using electron tomography [J]. Corrosion Science, 2012, 58: 299−306.

[16] BOAG A, TAYLOR R J, MUSTER T H, GOODMAN N, MCCULLOCH D, RYAN C, ROUT B, JAMIESON D, HUGHES A E. Stable pit formation on AA2024-T3 in a NaCl environment [J]. Corrosion Science, 2010, 52: 90−103.

[17] LIU D Y, LI J F, MA Y L, GUPTA R K, BIRBILIS N, ZHANG R. A closer look at the role of Zn in the microstructure and corrosion of an Al−Cu−Li alloy [J]. Corrosion Science, 2018, 145: 220−231.

[18] ZHANG X, ZHOU X, MA Y, THOMPSON G E, LUO C,

SUN Z, ZHANG X, TANG Z. The propagation of localized corrosion in Al−Cu−Li alloy [J]. Surface and Interface Analysis, 2016, 48: 745−749.

[19] ZHANG Xin-xin, ZHOU Xiao-rong, HASHIMOTO T, LINDSAY J, CILLCA O, LUO Chen, SUN Zhi-hua, TANG Zhi-hui. The influence of grain structure on the corrosion behaviour of 2A97-T3 Al−Cu−Li alloy [J]. Corrosion Science, 2017, 116: 14−21.

[20] WEN Feng, CHEN Ji-qiang, HAN Shuang, YE Jie-yun, REN Jie-ke, ZHANG Ying-hui, LI Wei-rong, GUAN Ren-guo. The initial corrosion behavior of Al−Cu−Li bicrystals: Effect of misorientation and precipitates [J]. Journal of Materials Research and Technology, 2022, 18: 3716−3724.

[21] LIU Dan-yang, SANG Feng-jian, LI Jin-feng, BIRBILIS N, WANG Zhi-xiu, MA Yun-long, ZHANG Rui-feng. The role of grain structure characteristics on the localised corrosion feature in the 1445 Al−Cu−Li alloy [J]. Materials Characterization, 2019, 158: 109981.

[22] ZHANG Xin-xin, LV You, LIU Bing, ZHOU Xiao-rong, ZHANG Tong, GAO Yi-han, DONG Ze-hua, WANG Jun-jie, NILSSON J O. The influence of room temperature storage on intergranular corrosion susceptibility of AA6082 Al−Mg−Si alloy [J]. Corrosion Communications, 2021, 3: 71−79.

[23] ZHANG Xin-xin, ZHOU Xiao-rong, NILSSON J O, DONG Ze-hua, CAI Chang-run. Corrosion behaviour of AA6082 Al−Mg−Si alloy extrusion: Recrystallized and non-recrystallized structures [J]. Corrosion Science, 2018, 144: 163−171.

[24] XU W, XIN Y C, ZHANG B, LI X Y. Stress corrosion cracking resistant nanostructured Al−Mg alloy with low angle grain boundaries [J]. Acta Materialia, 2022, 225: 117607.

[25] LIM M L C, KELLY R G, SCULLY J R. Overview of intergranular corrosion mechanisms, phenomenological observations, and modeling of AA5083 [J]. Corrosion, 2015, 72: 198−220.

[26] ZHANG Xin-xin, LV You, HASHIMOTO T, NILSSON J O, ZHOU Xiao-rong. Intergranular corrosion of AA6082 Al−Mg−Si alloy extrusion: The influence of trace Cu and grain boundary misorientation [J]. Journal of Alloys and Compounds, 2021, 853: 157228.

[27] ZHANG Xin-xin, JIAO Yan-bin, YU Yang, LIU Bing, HASHIMOTO T, LIU Hong-fang, DONG Ze-hua. Intergranular corrosion in AA2024-T3 aluminium alloy: The influence of stored energy and prediction [J]. Corrosion Science, 2019, 155: 1−12.

[28] ZHANG Yu-peng, LV You, LIU Er-gen, CAI Guang-yi, PAN Qing-lin, LIU Bing, DONG Ze-hua, ZHANG Xin-xin. Corrosion morphology evolution in 2A97-T6 Al−Cu−Li alloy: The influence of grain-stored energy [J]. Materials Characterization, 2022, 191: 112169.

[29] MA Yan-long, XU Hui-bin, LIANG Zhao-yuan, LIU Lei. Corrosion resistance of friction stir welded Al–Cu–Li alloy AA2099-T8 [J]. Acta Metallurgica Sinica (English Letters), 2020, 33: 127−134.

[30] MA Y, ZHOU X, LIAO Y, YI Y, WU H, WANG Z, HUANG W. Localised corrosion in AA 2099-T83 aluminium−lithium alloy: The role of grain orientation [J]. Corrosion Science, 2016, 107: 41−48.

[31] ZHANG Xin-xin, ZHOU Xiao-rong, HASHIMOTO T, LIU Bing. Localized corrosion in AA2024-T351 aluminium alloy: Transition from intergranular corrosion to crystallographic pitting [J]. Materials Characterization, 2017, 130: 230−236.

[32] ZHANG Xin-xin, ZHOU Xiao-rong, HASHIMOTO T, LIU Bing, LUO Chen, SUN Zhi-hua, TANG Zhi-hui, LU Feng, MA Yan-long. Corrosion behaviour of 2A97-T6 Al−Cu−Li alloy: The influence of non-uniform precipitation [J]. Corrosion Science, 2018, 132: 1−8.

[33] KING P C, COLE I S, CORRIGAN P A, HUGHES A E, MUSTER T H, THOMAS S. FIB/SEM study of AA2024 corrosion under a seawater drop. Part II [J]. Corrosion Science, 2012, 55: 116−125.

[34] BUCHHEIT R G, MARTINEZ M A, MONTES L P. Evidence for Cu ion formation by dissolution and dealloying the Al_2CuMg intermetallic compound in rotating ring-disk collection experiments [J]. Journal of the Electrochemical Society, 2000, 147: 119−124.

[35] BUCHHEIT R G, GRANT R P, HLAVA P F, MCKENZIE B, ZENDER G L. Local dissolution phenomena associated with *S* phase (Al_2CuMg) particles in aluminum alloy 2024-T3 [J]. Journal of the Electrochemical Society, 1997, 144: 2621−2628.

[36] MA Yan-long, ZHOU Xiao-rong, MENG Xiao-min, HUANG Wei-jiu, LIAO Yi, CHEN Xiao-li, YI Ya-nan, ZHANG Xin-xin, THOMPSON G E. Influence of thermomechanical treatments on localized corrosion susceptibility and propagation mechanism of AA2099 Al−Li alloy [J]. Transactions of Nonferrous Metals Society of China, 2016, 26: 1472−1481.

[37] ZHANG Xin-xin, LIU Bing, ZHOU Xiao-rong, WANG Jun-jie, LUO Chen, SUN Zhi-hua, TANG Zhi-hui, LU Feng. Corrosion behavior of friction stir welded 2A97 Al−Cu−Li alloy [J]. Corrosion, 2017, 73: 988−997.

[38] GLENN A M, MUSTER T H, LUO C, ZHOU X, THOMPSON G E, BOAG A, HUGHES A E. Corrosion of AA2024-T3. Part III: Propagation [J]. Corrosion Science, 2011, 53: 40−50.

[39] BOAG A, HUGHES A E, GLENN A M, MUSTER T H, MCCULLOCH D. Corrosion of AA2024-T3. Part I: Localised corrosion of isolated IM particles [J]. Corrosion Science, 2011, 53: 17−26.

[40] ZHANG Xin-xin, LIU Bing, ZHOU Xiao-rong, WANG Jun-jie, HASHIMOTO T, LUO Chen, SUN Zhi-hua, TANG Zhi-hui, LU Feng. Laser welding introduced segregation and its influence on the corrosion behaviour of Al−Cu−Li alloy [J]. Corrosion Science, 2018, 135: 177−191.

[41] ORŁOWSKA M, URA-BIŃCZYK E, OLEJNIK L, LEWANDOWSKA M. The effect of grain size and grain boundary misorientation on the corrosion resistance of commercially pure aluminium [J]. Corrosion Science, 2019, 148: 57−70.

[42] GARCIA-VERGARA S, COLIN F, SKELDON P, THOMPSON G E, BAILEY P, NOAKES T C Q, HABAZAKI H, SHIMIZU K. Effect of copper enrichment on the electrochemical potential of binary Al−Cu alloys [J].

Journal of the Electrochemical Society, 2004, 151: 16−21.
[43] AKIYAMA E, ZHANG Z G, WATANABE Y, TSUZAKI K. Effects of severe plastic deformation on the corrosion behavior of aluminum alloys [J]. Journal of Solid State Electrochemistry, 2009, 13: 277−282.
[44] MIYAMOTO H. Corrosion of ultrafine grained materials by severe plastic deformation: An overview [J]. Materials Transactions, 2016, 57: 559−572.
[45] MIYAMOTO H, YUASA M, RIFAI M, FUJIWARA H. Corrosion behavior of severely deformed pure and single-phase materials [J]. Materials Transactions, 2019, 60: 1243−1255.

准原位分析 2A97 Al−Cu−Li 合金在不同热机械条件下的腐蚀行为

吕 由，孟祥喆，李岩岩，董泽华，张欣欣

华中科技大学 化学与化工学院 材料化学与服役失效湖北省重点实验室，武汉 430074

摘 要：2A97 Al−Cu−Li 合金在航空工业领域具有十足的发展前景，但其表现出的高腐蚀敏感性限制其更广泛的应用。本文作者采用冷加工和时效工艺，在不同热机械条件下制备 2A97 Al−Cu−Li 合金，以阐明析出相和晶格储存能对其局部腐蚀演变的影响。结合准原位分析、传统浸泡试验和电化学测量，研究 2A97 合金的腐蚀行为。结果表明：析出相显著影响腐蚀尖端的铜富集现象，从而显著影响铝合金的腐蚀敏感性；而晶格储存能的分布则与局部腐蚀扩展密切相关。准原位分析不仅表现出与传统浸泡测试相当的腐蚀规律，还可提供具有更高时间和空间分辨率的组织结构演化信息，因而被视作一种探索局部腐蚀微观机制的有效方法。

关键词：Al−Cu−Li 合金；腐蚀行为；准原位分析；晶格储存能；热机械处理

(Edited by Wei-ping CHEN)